Lawrence Berkeley National Laboratory
LBL Publications

Title
Reactive Transport Modeling of Mineral Precipitation and Carbon Trapping in Discrete Fracture Networks

Authors
Steefel, Carl I
Hu, Mengsu

Water Resources Research®

Key Points:

- Modeling of the interplay between intersecting rough fracture networks and advection, gas diffusion, and mineral dissolution/precipitation
- Mineral precipitation due to mixing at fracture intersections can alter the flow connectivity of a fracture network
- Modeling demonstrates CO_2 trapping in naturally fractured rocks within the critical zone, a base case for engineered technologies

Correspondence to:

C. I. Steefel,
CISteefel@lbl.gov

Author Contributions:

Conceptualization: Carl I. Steefel, Mengsu Hu
Formal analysis: Mengsu Hu
Funding acquisition: Carl I. Steefel
Methodology: Carl I. Steefel, Mengsu Hu
Project Administration: Carl I. Steefel
Software: Carl I. Steefel, Mengsu Hu
Visualization: Carl I. Steefel, Mengsu Hu
Writing – original draft: Carl I. Steefel, Mengsu Hu
Writing – review & editing: Carl I. Steefel, Mengsu Hu

Reactive Transport Modeling of Mineral Precipitation and Carbon Trapping in Discrete Fracture Networks

Carl I. Steefel[1] and **Mengsu Hu[1]**

[1]Energy Geosciences Division, Lawrence Berkeley National Laboratory, Berkeley, CA, USA

Abstract In this study we use numerical experiments to analyze reactive flow and transport behavior in discrete intersecting fracture networks, focusing on (a) how reaction-induced changes in physical and chemical properties affect flow connectivity and (b) how fracture networks developed in the Earth's critical zone contribute to carbon sequestration via mineral weathering reactions. In the first part of the study, we used two-dimensional reactive flow and transport simulations to analyze the impacts of mixing in a natural discrete fracture network. We concluded that reaction-induced changes can substantially alter the flow connectivity, especially at fracture intersections. The second set of simulations considered the problem of natural weathering of fractured mafic and ultramafic rocks in the partially saturated Earth's critical zone as a function of infiltration rates, fracture permeability, and partially saturated flow parameters. As a model system, we considered an incongruent reaction network with dissolution of forsterite and precipitation of magnesite. The behavior is complex in terms of the rate-controlling processes because of the multicomponent nature of the system as shown by the grid Peclet number: the CO_2 behavior is gas diffusion-controlled in the partially saturated zone, while the rate of water flow via the Damköhler number controls Mg^{2+} transport through the fracture network. The amounts of carbon that can be trapped are modest, but the naturally fractured domain considered here provides a useful "base case" against which various engineered solutions can be compared.

Plain Language Summary In this study we use numerical experiments to analyze reactive flow and transport behavior in discrete intersecting fracture networks, focusing on (a) how the interplay between intersections of rough fractures and advection, diffusion, and chemical reaction affects flow connectivity via changes in geometry and physical and chemical properties and (b) how fracture networks developed in the Earth's critical zone contribute to carbon sequestration via mineral weathering reactions. In the first part of the study, we used reactive flow and transport simulations to analyze the impacts of mixing in a natural discrete fracture network. We concluded that reaction-induced changes can substantially alter the flow connectivity, especially at fracture intersections. The second set of simulations considered the problem of natural weathering of fractured mafic and ultramafic rocks in the partially saturated Earth's critical zone as a function of infiltration rates, fracture permeability, and partially saturated flow parameters. The behavior is complex in terms of the rate-controlling processes because of the multicomponent nature of the system. The amounts of carbon that can be trapped are modest, but the naturally fractured domain considered here provides a useful "base case" for the future design of efficient strategies for carbon trapping and mitigation.

1. Introduction

The critical role of fractures in governing the flow of fluid and the transport of chemical constituents in soils, sediments, and rock formations is increasingly recognized. In many near-surface and subsurface geomaterials, particularly those with relatively low permeability, fractures account for the bulk of the transmissivity because flow in the rock matrix is typically considered to be negligible. In Earth systems, fractures govern the safety and/ or the efficiency of energy recovery and storage in the subsurface such as CO_2 sequestration, geothermal exploration, and energy storage (Hu & Rutqvist, 2020, 2022). Fractures also play a crucial role in processes in shallow groundwater systems where their control on transport rates can influence drinking water quality (Berkowitz, 2002; Blessent et al., 2014; Chambon et al., 2010; F. Chen et al., 2012; Q. Hu et al., 2002), and in the Earth's critical zone, where they affect greenhouse gas cycling, soil development, CO_2 mitigation, and plant processes (Brantley et al., 2007; Dixon et al., 2009; Rempe & Dietrich, 2014). With sizes ranging from microns to kilometers, fractures may act as conduits or seals for fluid flow in the near-surface and subsurface systems. For subsurface energy recovery (e.g., hydrocarbon recovery and geothermal exploitation), effectively increasing permeability through a fracture network by using coupled hydro-mechanical (e.g., hydraulic fracturing, hydro-shearing), and chemical

(e.g., acid fracturing) processes is the key for efficient production. In the gas storage systems, fractures may act as unwanted flow conduits that may compromise the seal integrity of the storage facility. On the other hand, natural fractures with rough surfaces may provide reactivity for mineral trapping of carbon.

Comparing the near-surface and surface environments, the intrinsic geometric patterns of fractures and the coupled processes taking place in both are similar. The major differences in these two types of systems are stress conditions, temperature, and the nature of the gas phase if present. Fluid flow in the near-surface can be complicated due to the occurrence of partially saturated conditions (Boisson et al., 2015; Brantley et al., 2007; Novitsky et al., 2018; Owen et al., 2007; Shapiro et al., 2007). In terms of chemical reactions, redox processes are typically more important in near-surface environments like the Earth's critical zone due to the influx of O_2 gas from the atmosphere.

Despite these differences in coupled hydrological, mechanical, chemical, and thermal processes conditions in the near-surface and subsurface, a few intrinsic similarities exist. CO_2 gas, for example, may play an important role in both environments—derived from the atmospheric and soil respiration in the Earth's critical zone, and from deep geologic or anthropogenic sources in the subsurface. The geometric patterns of fractures appear to be similar based on field observation and laboratory experiments at different scales. This can be explained by similar types of coupled processes that lead to the creation and alteration of fractures. In addition, similar types of physical and chemical processes occur that can be described with similar conservation laws and physical laws (Hu & Rutqvist, 2020). Because of these similarities, it can be effective in some cases to use the same modeling and/or experimental approaches to investigate the interplay of discrete fracture networks and coupled processes.

Chemically-induced changes in fractures, especially those leading to permeability increase or decrease, are typically driven by flow within the fractures themselves, although interaction with the rock matrix may be important in some cases (Steefel & Lichtner, 1994). The reaction-induced fracture evolution is driven by the influx of fluids out of equilibrium with respect to the mineralogy within the fracture itself, and in some cases a relatively narrow portion of the rock matrix bordering the fracture (Steefel & Lichtner, 1998). Dissolution of the minerals in the fractures may lead to porosity and permeability increase, but it is also possible that fracture asperities that keep the fracture open may dissolve, thus leading to permeability decrease where sufficient stress is present to force the fracture to close (Ameli et al., 2014; Detwiler, 2008). Pressure solution processes within the fracture, with or without flow, may also lead to corrosion of asperities and fracture closing (M. Hu, Steefel, & Rutqvist, 2021).

A lesser number of modeling studies have addressed the problem of mineral precipitation leading to fracture clogging, but a few are noteworthy (Singurindy & Berkowitz, 2005; Steefel & Lasaga, 1994; Steefel & Lichtner, 1998). For mineral precipitation to occur, supersaturation of the fluid flowing through the fracture is required. This can be due either to regional chemical, thermal, or hydrological effects, mixing between different groundwaters, or the result of local dissolution-precipitation (incongruent) reactions where secondary reaction products have a larger volume than the reactants. Steefel and Lasaga (1994) discussed the case of fracture sealing due to flow of silica-rich fluids down a temperature gradient and suggested based on their simulations that it might be possible to cause wholesale reorganization of the hydrothermal convection cell if sufficient fracture clogging occurred. Interaction of shallow groundwater with naturally occurring cementitious zones at the Maqarin site in Jordan were predicted to result in fracture sealing, in agreement with observations (Steefel & Lichtner, 1998). Other studies pointed to the important role of the rock matrix in providing chemical fluxes to the fracture where precipitation could occur (Steefel & Lichtner, 1994).

Previous studies focusing on the role of mineral precipitation on fracture permeability considered relatively simple models based on a set of parallel fractures with permeability described by the cubic law (Steefel & Lasaga, 1994; Steefel & Lichtner, 1998; Witherspoon et al., 1980; Zimmerman & Bodvarsson, 1996). Fewer studies have considered intersecting fracture networks (M. Hu et al., 2016, 2017; Hyman & Jiménez-Martínez, 2018), and only one to our knowledge has considered mineral precipitation or coupled mineral dissolution and precipitation in these environments (Feng et al., 2019). More studies have focused on characterization of intersecting fracture networks in which precipitation has occurred, including Crandall et al. (2017).

A large number of numerical models have been applied to analyze fluid flow (M. Hu et al., 2016; Hyman & Jiménez-Martínez, 2018), mechanics (M. Hu et al., 2017), and hydro-mechanical (Hu & Rutqvist, 2020, 2022; M. Hu et al., 2017, Hu, Rutqvist, & Steefel, 2021) processes in discrete fracture networks. A recent review paper by Laubach et al. (2019) highlights many of the important topics with regard to fractured rock systems, and they

note that the topic of mineral precipitation in these systems is relatively neglected. Noiriel et al. (2021) considered mineral precipitation in fractured rock, but did not consider the role of mixing (fractures split rather than converge), or that of gas phase transport. Jones and Detwiler (2019) examined precipitation in a single fracture, although they did not consider the role of mixing or gas phase transport as is done in this study. Here we use numerical experiments involving coupled processes involving advection, gas diffusion, mineral dissolution, and precipitation to investigate the following scientific question:

How does mineral precipitation driven by chemical reaction, advection, and gas diffusion interplay with the geometry of natural discrete fracture networks, particularly at intersections where coupling of chemical and physical processes is most important?

In this study, we investigate reactive transport in discrete rough intersecting fracture networks leading to precipitation of secondary carbonate phases. The scale that is considered in this study is on the order of meters, although the results should be applicable to smaller and larger scale systems with adjustment for the width and permeability of the fracture zones. We consider two scenarios related to carbon mineralization: (a) the case where fluid mixing provides the necessary supersaturation for carbonate precipitation, and (b) the case where dissolution of a primary silicate mineral provides the divalent ion (Ca^{2+}, Mg^{2+}, or Fe^{2+}) needed for supersaturation of the secondary carbonate phase. For the first case, mixing of CO_2-rich and Mg^{2+}-rich fluids at fracture intersections results in supersaturation with respect to the mineral magnesite, which then precipitates according to well-established kinetic rate laws (Giammar et al., 2005; Hänchen et al., 2006; Steefel & Yang, 2021; Wang & Giammar, 2013). For the second case, we consider the reaction of CO_2-rich fluid with the mineral forsterite (Mg-olivine). The forsterite to magnesite conversion has been studied extensively (Giammar et al., 2005; Steefel & Yang, 2021; Xiong & Giammar, 2014) and is used here as a proxy for more common rock types like basalt and various ultramafic rocks (Xiong et al., 2018). The comparison with basalt is limited of course because of the lack of iron in the forsteritic olivine phase, but for the purposes of focusing on the interplay between the of intersecting fracture networks and coupled physical and chemical processes, the simpler mineralogy is an advantage.

We begin with (a) flow in a subsurface fracture network within which only single-phase flow occurs, and then (b) progress to a fracture network developed in the Earth's critical zone where partially saturated flow and transport are relevant. For the subsurface single-phase flow example, a single initial permeability is adopted for the discrete fracture zone with the assumption that the fracture itself is filled with crushed and granulated material such that it can be considered locally as a porous medium. Mineral precipitates that accumulate in the pore space of the fracture gradually reduce the permeability. This example is used primarily to investigate the effects of fluid mixing in intersecting fractures. The role of diffusive exchange with the rock matrix is not emphasized in this study for several reasons. First, the rock matrix permeability and diffusivity are assumed to be very low in this study so that the focus is on reactive material within the fracture zone itself. Second, to have significant impact on the system behavior, the rock matrix would have to be different mineralogically from the fracture filling, for example, such that small scale chemical gradients develop along the fracture edge. For the partially saturated example, we use an aperture-based permeability law where the arbitrary distribution of the natural fracture asperities is rigorously considered. The latter environment has implications for the effectiveness of natural and enhanced weathering (or negative emission) approaches to atmospheric CO_2 mitigation.
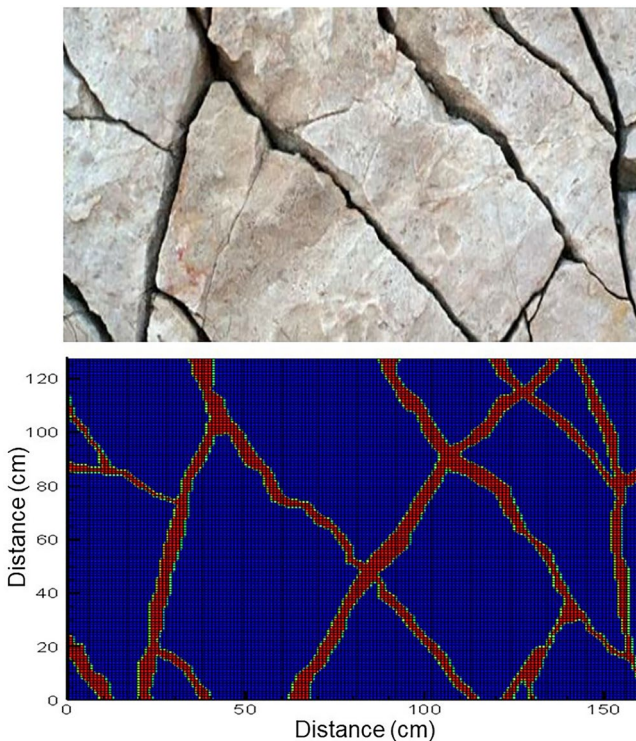

Figure 1. Top, photograph showing intersecting rough fractures in granite (top). Bottom, computational grid developed from the photograph, with an additional fracture added to increase the interest of the simulation. The mixing simulations discussed below consider a horizontal domain measuring 160 by 128 cm with a uniform grid spacing of 1 cm. The critical zone simulation grid (not shown here) considers a vertical domain measuring 200 cm in Z (height) and 62 cm in X discretized with 1.0 and 0.25 cm spacing respectively.

2. Approach

The reactive transport behavior of intersecting fracture networks was investigated in 2D with the software CrunchFlow (Steefel et al., 2015). CrunchFlow (or CrunchTope) is a general-purpose multicomponent reactive transport
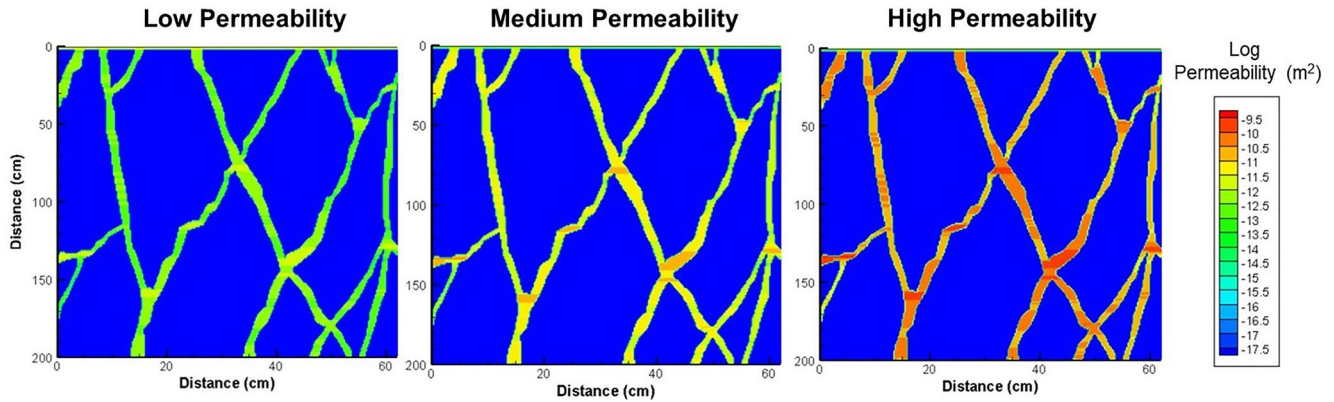
Figure 2. Log absolute permeability values in m^2 based on the cubic law for three different fracture porosities: 10^{-4}, 10^{-3}, and 10^{-2} (see Equation 8) used in partially saturated critical zone simulations).

simulator that handles advective, diffusive, and dispersive transport, and an arbitrary number of mixed equilibrium and kinetic reactions. CrunchFlow is able to simulate single-phase flow in heterogeneous domains, including fracture flow (e.g., Steefel & Lichtner, 1998). More recently, the capability to simulate partially saturated flow based on a predictor-corrector treatment of the Richards equation (Li et al., 2021) has been added to the code.

Using a photograph of fractured granite (Figure 1, top), we added an additional fracture to increase the interest of the simulation (computational grid shown in Figure 1, bottom). The same fractured rock was considered previously by Hu and Rutqvist (2022). The fractures are conceptualized as a set of segments with arbitrary distributions of asperities along the fractures in 2D into the plane of Figure 1. Thus, as in Steefel and Lichtner (1994) and Steefel and Lichtner (1998), the interface between the fractures and the adjacent rock matrix is a plane into the page.

2.1. Reactive Transport Approach

The reactive transport equations are the same for the two scenarios (mixing and partially saturated) considered here. Using the software CrunchFlow (Steefel et al., 2015), we solve numerically the following multicomponent equation:

$$\frac{\partial \left(\phi S_L C_{i,\text{aq}} + \phi S_G C_{i,g} \right)}{\partial t} = \nabla \cdot \left(\phi S_L D_i^{\text{aq}} \nabla C_{i,\text{aq}} \right) + \nabla \cdot \left(\phi S_G D_i^{g} \nabla C_{i,g} \right)$$
$$- \nabla \cdot \left(\phi S_L \upsilon C_{i,\text{aq}} \right) - \sum_{r=1}^{N_r} \upsilon_{ir} R_r - \sum_{m=1}^{N_m} \upsilon_{im} R_m - \sum_{l=1}^{N_g} \upsilon_{il} R_l$$

(1)

where $C_{i,\text{aq}}$ and $C_{i,g}$ are the concentrations of the ith species in the aqueous (liquid) and gas phases respectively, ϕ is the porosity, S_L and S_G are the liquid and gas saturation respectively, D_i^{aq} and D_i^{g} are the diffusion coefficients in the aqueous and gas phases respectively, υ is average linear velocity, υ_{ir}, υ_{im}, and υ_{il} are the stoichiometric coefficients for N_r aqueous reaction, N_m mineral reactions, and N_l gas reactions at R_r, R_m, and R_l rates, respectively.

For mineral dissolution and precipitation, a transition state theory (TST) type rate law is used to describe both magnesite and forsterite:

$$R_m = -A_m k_m \left[1 - \frac{Q}{K_{eq}} \right]$$

(2)

where A_m is the reactive surface area (m^2 m^{-3}), k_m is the rate constant (mol m^{-2} s^{-1}), and the convention used is that the rate is positive in the case of precipitation.

The porosity ϕ is updated according to the evolving mineral volume fractions ϕ_m as a result of reaction according to
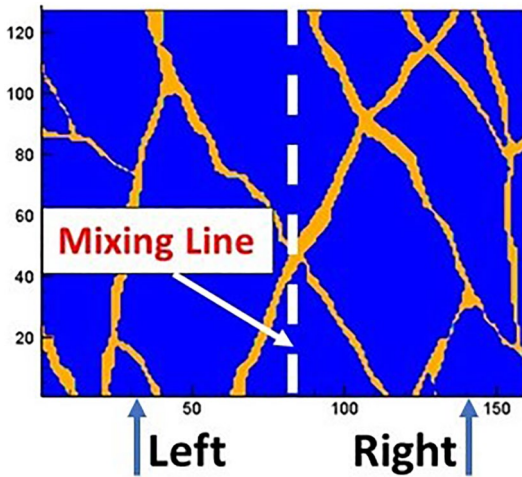
Figure 3. Schematic of computational domain showing a discrete rough fracture network and the mixing line in dashed white. Differing geochemical boundary conditions are used along the lower boundary on either side of the dashed white line. Flow is from bottom to top.

$$\phi = 1 - \sum_1^{N_m} \phi_m \tag{3}$$

2.2. Flow Simulations

Two differing formulations for calculating flow velocities based on Darcy's Law are used in the simulations that follow. In the first where the focus is on mixing in a general subsurface environment, we simulate single phase flow with the assumption that the fracture zones shown in Figure 1 consist of coarsely crushed rock that can be described with a single initial permeability. In the second, we focus on the behavior of fracture networks in the critical zone where it is necessary to solve the Richards equation so as to account for the partially saturated conditions. In the critical zone case, we use a formulation for fracture permeability based on a modified cubic law (e.g., Witherspoon et al., 1980) in which the fracture zone is assumed to consist of a set of segments with different apertures due to the arbitrary distribution of the asperities along the fractures. The purpose of using different permeability models for the different sets of problems is to explore the choices of using cubic law and porosity-permeability models.

2.2.1. Single-Phase Flow Simulations to Investigate Mixing

The first set of simulations investigating the role of fluid mixing is based on a computational domain measuring 160 by 128 cm and uses a constant 1 cm grid spacing (Figure 1, bottom). In these simulations, the fractures are zones consisting of an initial permeability of 10^{-13} m^2 that contrast with the rock matrix permeability of 2.5×10^{-19} m^2. The value for permeability of the fracture zone is close to what has been reported for fractures and shear zones at Yucca Mountain by Y. F. Chen et al. (2022) (about 5.0×10^{-13} m^2 for Yucca Mountain, see their Table 3). Following the approach in many subsurface treatments, the mixing simulations consider only single-phase flux, q, described with the classical Darcy's Law:

$$q = -\frac{k}{\mu}(\nabla p) \tag{4}$$

where k and μ are the permeability and dynamic viscosity. In the simulations in which the porosity evolves due to geochemical reactions, the permeability is updated according to:

$$k = k_0 \frac{\phi^3}{\phi_0^3} \tag{5}$$

where k is the permeability and k_0 and ϕ_0 are the initial permeability and porosity, respectively. Darcy's Law is used to calculate the flow velocities, satisfying $q = \phi v$. In the single flow simulations, the initial porosity of the fractures is assumed to be 0.20. Combining Equations 1–5, we consider advection, multicomponent diffusion and chemical reaction in fractured porous rocks where the permeability can be modified due to changes of porosity as a result of chemical reaction. The initial porosity of the matrix block is assumed to be 1%.

2.2.2. Partially Saturated Flow Simulations in the Critical Zone

In a second set of simulations involving partially saturated flow in the critical zone, we consider a domain measuring 62 cm in X (width) and 200 cm in Y (depth) with a spacing of 0.25 and 1.0 cm in the X and Z coordinate directions respectively. Z in this case is parallel to the gravitational vector. In these simulations, we use the cubic law (M. Hu et al., 2016; Hu & Rutqvist, 2020; Witherspoon et al., 1980; Zimmerman & Bodvarsson, 1996; Zimmerman & Yeo, 2000) to describe a permeability that is a function of the hydraulic aperture b of a fracture segment:

$$k = \frac{b^2}{12} \tag{6}$$

Table 1

Geochemical Boundary Conditions Used on Lower Boundary for Mixing Simulation

	Left boundary	Right boundary	Initial
pH	7.8	8.2	7.5
pCO_2 (bars)	0.02	0.0005	0.0003
Mg^{++} (M)	0.0001	0.0008	0.00001
Na^+ (M)	0.1	0.1	0.1
Cl^- (M)	0.1	0.1	0.1
Forsterite saturation (log Q/K_{eq})	−9.367	−5.943	−14.545
Magnesite saturation (log Q/K_{eq})	−0.567	−0.457	−3.980

Note. Units for the magnesium, sodium, and chloride ions are in molarity (M).

Using directly the fracture widths shown in Figure 1 results in extremely high permeabilities, so we consider instead that the fracture zones in Figure 1 consist of a set of parallel fractures with apertures of 1% of the fracture zone widths mapped in Figure 1. Based on the smaller fractures developed in the fracture zone, we define a fracture porosity given by

$$\phi_F = \frac{b}{d} \tag{7}$$

where d is the fracture spacing (Figueiredo et al., 2017; Steefel & Lasaga, 1994). This results in a fracture transmissivity of

$$k = \phi_F \frac{b^2}{12} = \frac{b^3}{12d} \tag{8}$$

where in every case the fracture aperture b is 1% of the width of the fracture zone mapped from Figure 1. We consider values of the fracture porosity ϕ_F ranging from 10^{-4} to 10^{-2} (Figueiredo et al., 2017). The resulting permeability distributions are shown in Figure 2.

For the simulations intended to capture partially saturated conditions in the Earth's critical zone, the Richards equation is solved. A head form of the Richards equation is derived from the mixed form (Celia et al., 1990) by defining a specific capacity $C(h) = \partial\theta / \partial h$, which yields

$$\frac{\partial \theta}{\partial t} - \nabla \cdot [K(h)\nabla(h + z)] - q_s = 0 \tag{9}$$

where θ is the water content, h is the pressure head (i.e., $p/\rho g$), z is the elevation, $K(h)$ is the hydraulic conductivity, and S_s is the specific storage. The summation of h and z equals to hydraulic head. The hydraulic conductivity is related to the permeability by

$$K = \frac{\rho g k}{\mu} \tag{10}$$

where ρ and μ are the fluid density and dynamic viscosity, and g is the gravitational acceleration. Following the treatment in Li et al. (2021), the Mualem-van Genuchten model (Mualem, 1976; Van Genuchten, 1980) is used to link the pressure head with the water content and conductivity

$$S(h) = \left(1 + |\alpha h|^n\right)^{-m} \tag{11}$$

$$\theta(h) = \theta_r + (\theta_s - \theta_r)\, S(h) \tag{12}$$

$$K(h) = K_s S(h)^{1/2} \left[1 - \left(1 - S(h)^{1/m}\right)^m\right]^2 \tag{13}$$

where S is the saturation, α and m are soil parameters with $m = 1 - 1/n$, and θ_s and θ_r are the saturated and residual water contents, and K_s is the saturated hydraulic conductivity.

3. Results

3.1. Reaction-Induced Fracture Clogging Due To Mixing

In the simulations designed to investigate the role of fluid mixing in intersecting fractures, differing geochemical boundary conditions are used on either side of the dashed white mixing line along the lower boundary (Figure 3 and Table 1). Fractures (shown in tan) consist of higher permeability zones (10^{-13} m^2) cutting through lower permeability rock matrix (2.5×10^{-19} m^2). A net pressure gradient of 7,813 Pa/m was applied from bottom to top across the domain, with the X-Y domain considered to be perpendicular to the gravitational vector (i.e., no gravity effects on the advection). The sides of the

Table 2

Rate Constant and Reactive Surface Area for the Mixing Simulations

	Rate constant (k_m) mol m^{-2} s^{-1}	Reactive surface area (A_m) m^2 m^{-3}	Initial mineral volume fraction m^3 m^{-3}
Magnesite	10^{-8}	100	0.00

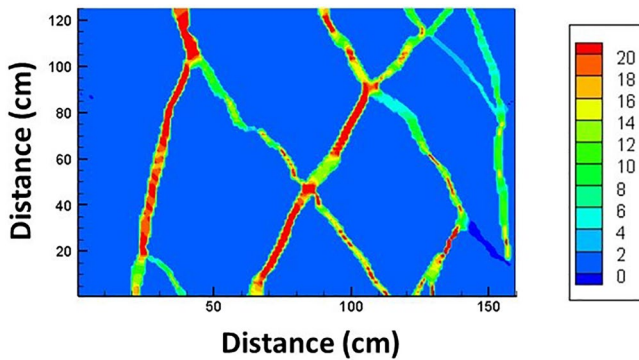**Figure 4.** Initial Y velocity distribution (m^3 m^{-2} yr^{-1}) in the fractures for the single-phase flow mixing case. The Y coordinate direction is oriented vertically, X is horizontal.

domain are considered no-flow, making the fractures along the left and right essentially dead-end pores. The aqueous diffusion coefficient is assumed to be 10^{-9} m^2 s^{-1} and a cementation exponent $m = 4.0$ is assumed for the rock matrix so as to define the tortuosity $\tau = \phi^m$. Thus, diffusive exchange with the rock matrix is included in the simulations, but the effect is minor because of the abundant reactive material assumed to be present in the fracture system itself, and because the rock matrix diffusivity is assumed to be low.

Two scenarios are considered: (a) a case in which both segments of the lower boundary are <-0.45 log Q/Keq with respect to magnesite, and (b) a case in which the left segment is close to equilibrium with respect to magnesite.

The geochemical boundary condition in Table 1 designated "Left" extends between 0 and 80 cm along the lower boundary, while the boundary condition designated "Right" extends from 80 to 160 cm. The boundary conditions are chosen to achieve magnesite supersaturation due to mixing between fractures originating from the left and right intersect at about 50 cm above the lower boundary.

Table 2 gives the kinetic parameters used in the simulations. The value for the magnesite rate constant is representative of what has been found in various experimental studies (e.g., Giammar et al., 2005; Steefel & Yang, 2021; Xiong & Giammar, 2014). The value for reactive surface area in the fractures represents a reasonable value for coarsely crushed material, which is then treated as an equivalent porous and permeable medium. Magnesite is allowed to form without a nucleation barrier according to the rate law given in Equation 2.

The permeability distribution shown in Figure 1 (bottom) and the net pressure head gradient of 7,813 Pa/m leads to a distribution of Y velocities shown in Figure 4. The variations in velocity along the extent of the fractures are due to the combination of the variable thickness of the fracture zones and the fluid mixing where two fractures join to form a single fracture, as in the upper left portion of the domain. Where two fractures intersect, the flow is split between the two fracture extensions, as in the intersecting fracture set at about 50 cm from the lower boundary in the Y direction along the mixing line shown in Figure 4.

In the first set of mixing simulations, magnesite is undersaturated along the entire length of the lower boundary (i.e., in both the "Left" and "Right" sectors shown in Figure 3; see Table 1). Thus, supersaturation is only achieved by mixing, which occurs primarily at the fracture intersection occurring at about $X = 80$ cm and $Y = 50$ cm.

Figure 5. Magnesite supersaturation (log Q/K_{eq}) developed above fracture intersection at approximately $X = 80$ cm and $Y = 50$ cm due to mixing. Flow is from bottom to top. The lower boundary is undersaturated with respect to magnesite.

The precipitation rate of magnesite over time is shown in Figure 6. The gradual reduction in the rate of precipitation is due to the clogging of the fracture segment over time, highlighting the important flow and transport control in this case.

The question arises whether the supersaturation developed on the upper right limb of the two intersecting fractures is a geochemical or flow effect? This can be easily tested by switching the geochemical boundary conditions in Table ("Left" and "Right"). When this is done, the supersaturation develops in the same area, indicating that the discrete zone of supersaturation is driven by the fracture flow characteristics rather than the geochemistry (result not shown). Similarly, in the next intersection at about $X = 110$ cm and $Y = 95$ cm, the magnesite precipitation rate is different in either segment following this intersection. The generalization here is that discrete fracture segments can develop distinct geochemical characteristics depending on the fracture geometry and fracture flow rates.

As with the magnesite saturation plot in Figure 5, switching the geochemical boundary conditions has no effect on the results. Thus, one concludes that the precipitation zone is controlled by the greater flux coming in from the fracture on the lower left, driving the reaction products to the right on the
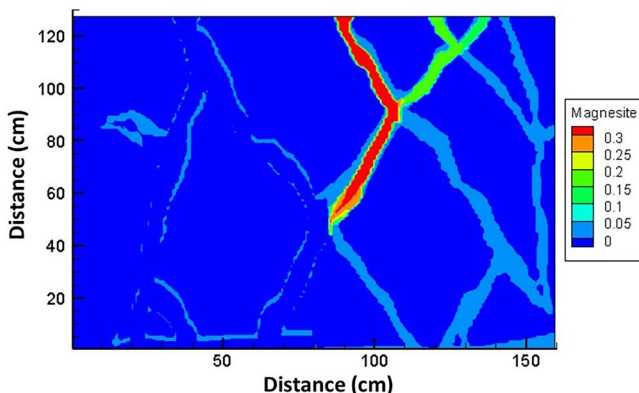
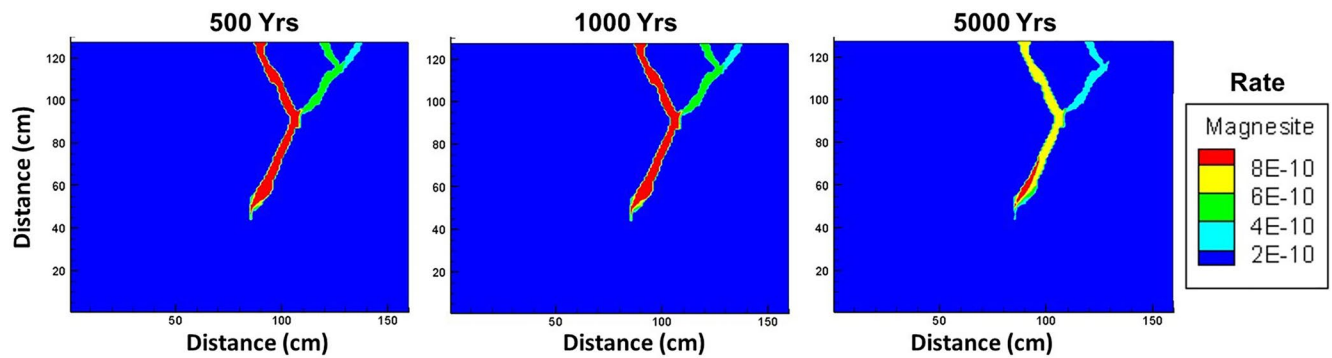**Figure 6.** Precipitation rate (mol m^{-3} s^{-1}) of magnesite over time driven by the supersaturation shown in Figure 4.

upper side of the fracture intersection. The precipitation of magnesite in the fracture causes a reduction in absolute porosity shown in Figure 7.

Since the resulting porosity change in the fracture zone is relatively small, the effects on permeability are similarly minor (Figure 8), although clearly detectable between 1,000 and 5,000 years.

As expected from the gradual decrease in permeability in the fracture segment above and to the right of the intersection at approximately $X = 80$ cm and $Y = 50$ cm, the flow velocity is gradually reduced selectively within the fracture segment where the magnesite precipitation occurs (Figure 9).

As discussed above, magnesite precipitation only occurs selectively in the right-hand segment of the fracture close to the intersection at 50 cm from the lower boundary. With the geochemical boundary conditions in Table 1 and the calculated flow velocities in the fractures, it is not possible to produce supersaturation and precipitation of magnesite on the left-hand side of the domain. To produce supersaturation and magnesite precipitation requires that the left-hand boundary be slightly supersaturated with respect to magnesite (Table 3). However, this boundary condition then only results in magnesite precipitation on the left side of the domain (Figure 10), and in this case mixing plays little role.
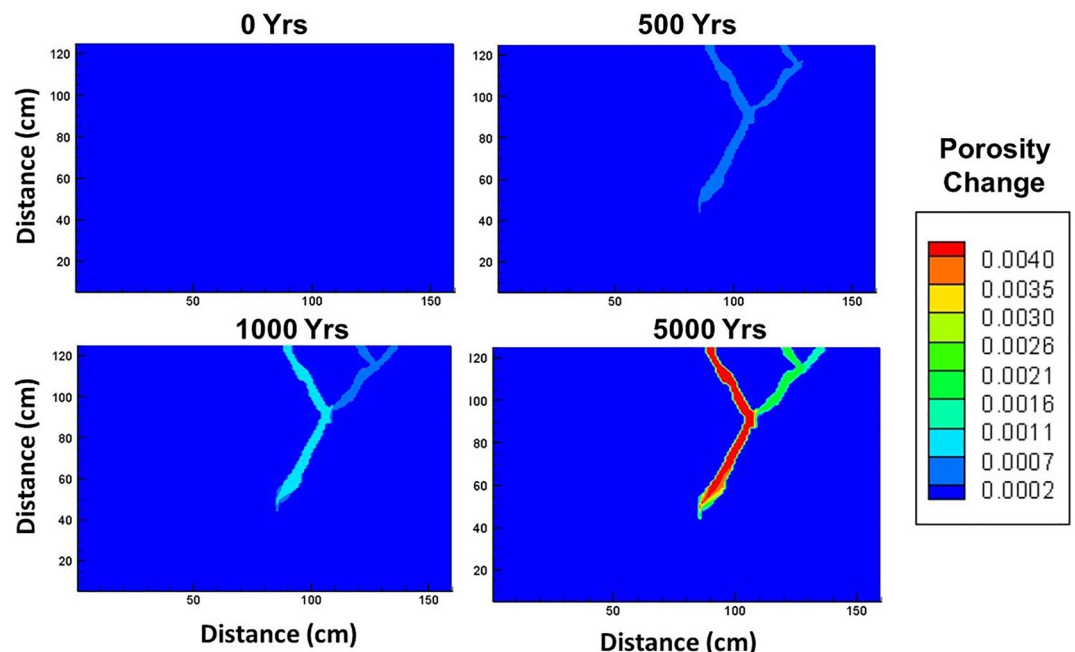

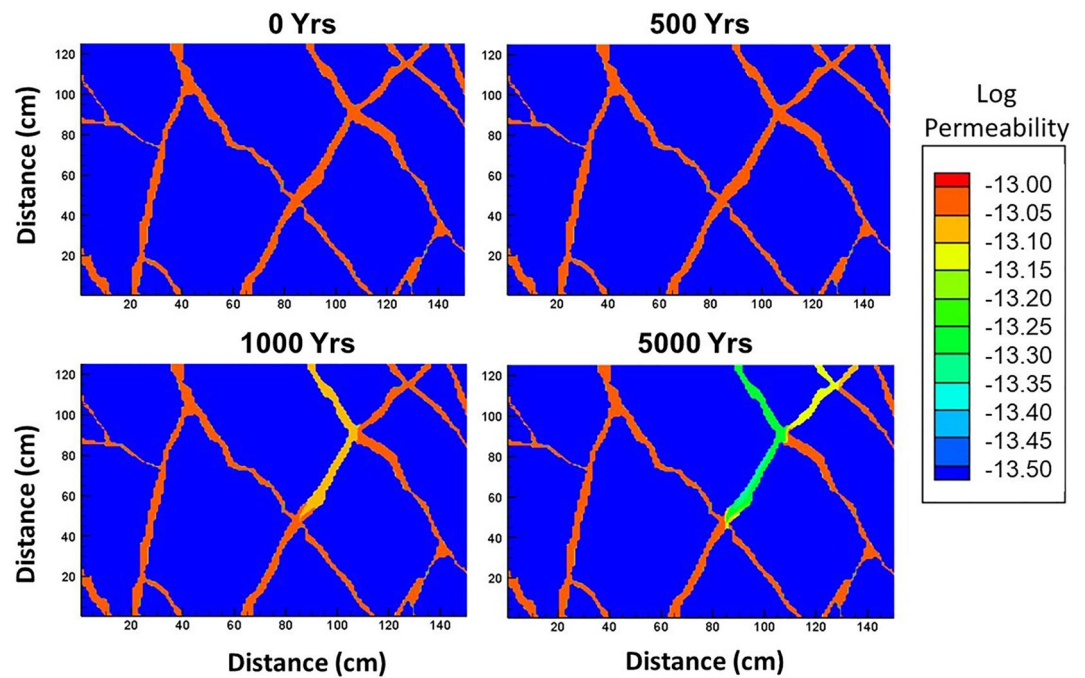**Figure 7.** Absolute change in porosity due to magnesite precipitation.

Figure 8. Evolution of the fracture permeability (m^2) to 5,000 years. The precipitation of magnesite in the right-hand fracture segment above the intersection at $Y = 50$ cm causes the permeability decrease.

3.2. Forsterite to Magnesite Weathering in the Partially Saturated Critical Zone

In recent years, a strong interest has developed in the topic of natural and enhanced weathering in soils and the Earth's critical zone as a way to mitigate increasing CO_2 gas concentrations in the atmosphere. For the case of natural weathering, fractured mafic and ultramafic rocks are obvious targets for mitigation of CO_2 because
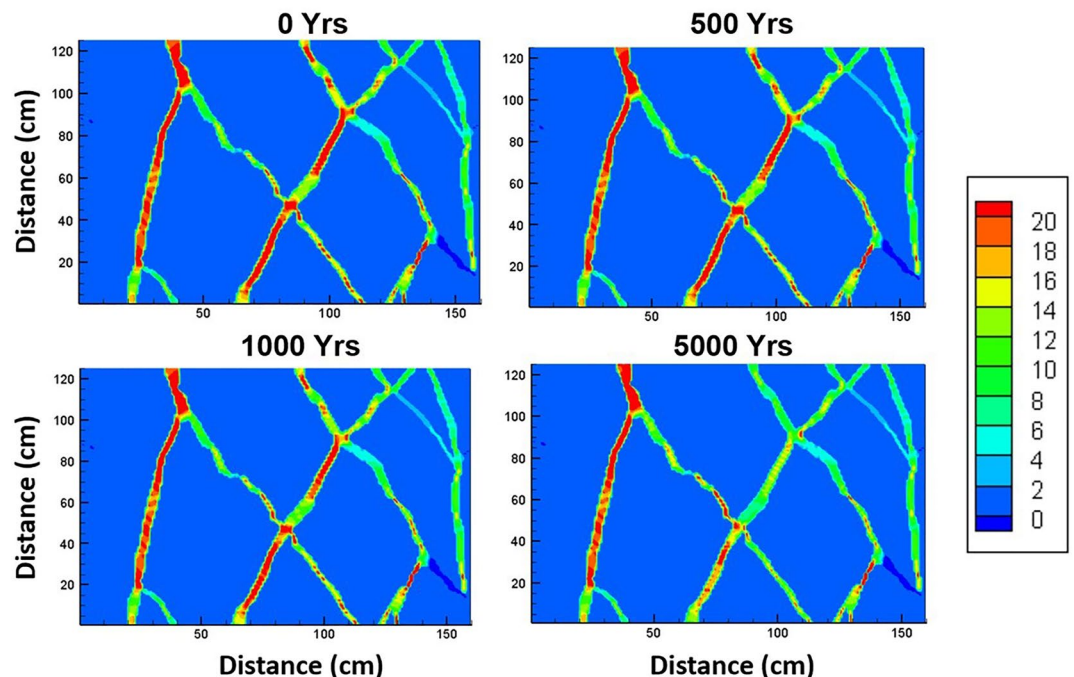

Figure 9. Evolution of the fracture flow Y velocities (m^3 m^{-2} yr^{-1}) for the single-phase flow mixing case. Y coordinate direction is oriented vertically, X is horizontal.

Table 3
*Geochemical Boundary Conditions for Mixing Case 2 Used on Lower Boundary*

	Left boundary	Right boundary	Initial
pH	7.8	8.0	7.5
pCO_2 (bars)	0.003	0.00075	0.0003
Mg^{++} (M)	0.001	0.001	0.00001
Na^+ (M)	0.1	0.1	0.1
Cl^- (M)	0.1	0.1	0.1
Magnesite saturation	0.004	−0.584	−3.980

Note. Units for the magnesium, sodium, and chloride ions are in molarity (M).

they are widespread on the globe and because they provide a ready source of cations (Ca^{2+}, Mg^{2+}, Fe^{2+}) for carbonate precipitation. Although a number of fundamental studies have considered reaction with basalt and various ultramafic rocks (Aradóttir et al., 2012; Beckingham et al., 2016, 2017; Xiong et al., 2018), their complexity in terms of reactive primary and secondary phases has been daunting. Thus, there has been interest in simpler geochemical and mineralogical systems that could serve as proxies for the mafic and ultramafic rocks. A good example is that of forsterite (Mg-olivine), which reacts with CO_2 to form magnesite (Steefel & Yang, 2021; Xiong & Giammar, 2014). Forsterite and similar mafic and ultramafic mineral phases are among those considered for engineered negative emission technologies (Campbell et al., 2022).

In the partially saturated (or vadose) zone within the shallow portions of the Earth's critical zone, infiltration of rainwater and snow melt combines with gas diffusion to drive acid-promoted and oxidative reactions that dissolve the primary mafic and ultramafic rock. The overall reaction is thus

$$\underbrace{Mg_2SiO_4}_{\text{Forsterite}} + 2CO_2 \rightarrow \underbrace{2MgCO_3}_{\text{Magnesite}} + SiO_2(aq) \tag{14}$$
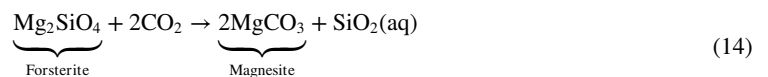
mediated by the presence of an aqueous phase.

The extent of carbonate precipitation in the case of either natural or enhanced weathering, although widely discussed in an engineering context, is poorly quantified. In particular, the rates of primary silicate dissolution and carbonate precipitation in partially saturated systems are poorly known—whether controlled by the rate of surface reaction or the rate of transport (water or gas) remains unknown. The important role of gas diffusion has long been recognized in soil and other critical zone (CZ) studies, since the rate of transport of the reactive constituent (e.g., O_2 or CO_2 gas) is typically greater in the gas phase (diffusion dominating) than in the aqueous phase
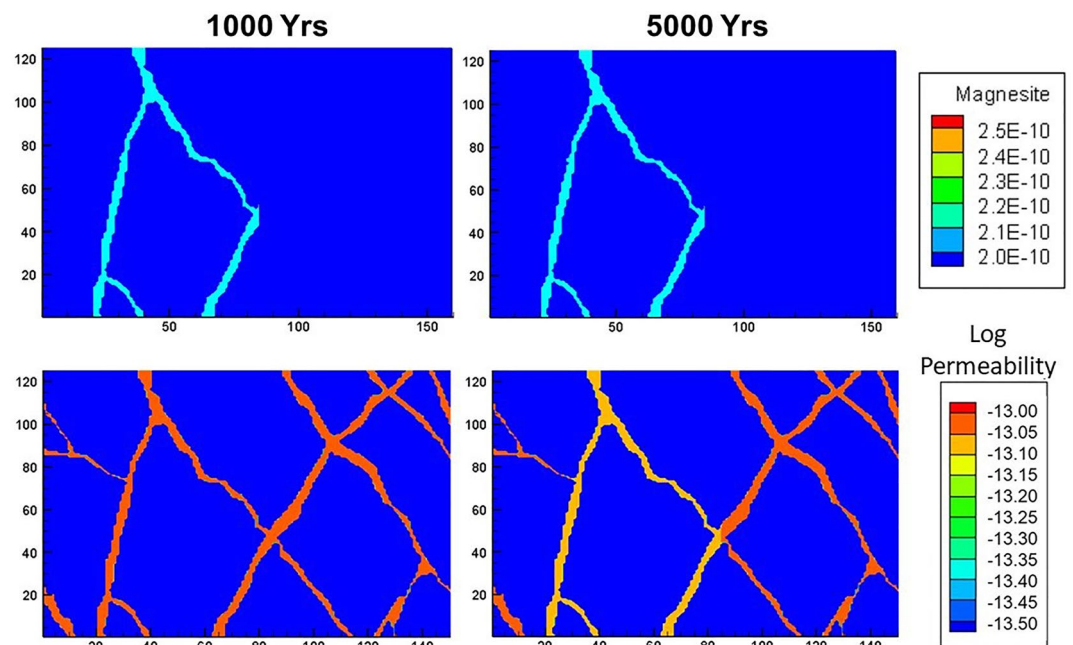

Figure 10. Simulations using geochemical conditions in Table 3, with the left-hand side of the lower boundary slightly supersaturated with respect to magnesite. Mixing on the right-hand side only serves to dilute the solution coming from the left side, thus preventing magnesite precipitation in this part of the domain altogether. Upper panel gives the magnesite rate in units of mol m^{-3} s^{-1}. Lower panel gives the value of the log permeability in m^2.

Table 4
Geochemical Boundary and Initial Conditions for Boundaries in the Earth's Critical Zone Simulations

	Top BC	Initial
pH	6.78	7.5
pCO_2 (bars)	0.02	00003
Mg^{++} (M)	0.001	0.001
Na^+ (M)	0.001	0.1
Cl^- (M)	0.001	0.1
Forsterite saturation	−11.962	−11.150
Magnesite saturation	−1.359	−2.282

Note. Units for the magnesium, sodium, and chloride ions are in molarity (M).

(both advection and diffusion). The lack of understanding and predictability is even more limited in the case of fractured rocks.

In the flow simulations that follow, we use a constant infiltration rate of 12.6 cm/year and consider three permeability levels designated "Lower," "Medium," and "Higher" corresponding to fracture porosities of 10^{-4}, 10^{-3}, and 10^{-2}, respectively (see Equation 8). For each of the three permeability levels, we assume a van Genuchten "n" of 2.80 based on the data compilation for fractured rocks from Yucca Mountain (Figure 5 in Y. F. Chen et al. (2022)). The fractured rocks at Yucca Mountain showed greater variation in terms of the van Genuchten (VG) α parameter (Figure 5, Y. F. Chen et al., 2022), so a range of values from 0.50 to 1.50 was used in the simulations. A residual water content $\theta_r = 0.10$ was assumed. The sides of the domain were assumed to be no-flow. The initial water table elevation was assumed to be at 50 cm depth. The top boundary is characterized with pressure at atmospheric values of 1 bar with a constant infiltration rate of 12.6 cm/year. The bottom boundary is set to a constant fixed head of 0.0 m and is assumed to be free drainage. The boundary and initial conditions are listed in Table 4, and the rate constants and reactive surface areas that are used in the simulations are listed in Table 5. It is important to note that in this set of simulations, we use a Z dimension to represent the gravity effects on the advection.

Since the fixed infiltration of water at 12.6 cm/year, all of the simulations gradually evolve to the same bulk flow rate through the fractured rock. However, the different distributions of gas and water, in the simulations resulting from the of different partially flow (or van Genuchten) parameters, can result in different reactivities.

Figure 11 shows the time evolution of the hydrological variables (liquid saturation and head) from 0.0365 to 0.365 to 3.65 days. The simulations for the three permeability cases show a gradual evolution toward steady state, with drainage of the fracture network dominating the early time behavior. The high permeability case appears to be closest to steady state by 3.65 days as the infiltration flux at the top of the system (free drainage at the bottom) establishes the flow through the fracture network. The medium and low permeability cases have not reached steady state by 3.65 days, as the drainage of the fracture network from the initial conditions (water table at 50 cm depth) dominates.

Given the presence of a partially saturated zone, it is important to include the process of gas diffusion, particularly in the case in which a reactive gas is important in the reaction network. To describe gas diffusion, we use the Millington-Quirk (Millington & Quirk, 1961) formulation for inclusion in Equation 1

$$D^g = S_G^{7/3} \phi^{1/3} D^{g,\text{intrinsic}} \tag{15}$$

in which S_G is the gas saturation and $D^{g,\text{intrinsic}}$ is the intrinsic gas diffusion coefficient taken as 10^{-6} m^2 s^{-1} in this study.

Figures 12–14 show the results of reactive flow and transport simulations for the three permeability cases respectively, with contour plots at 0.00365, 0.01825, 0.0365, 0.365, and 3.65 days (left to right) of the magnesite precipitation rate (mol m^{-3} s^{-1}) and liquid saturation.

The precipitation rates shown in Figures 12–14 reflect the coupling of forsterite dissolution and magnesite precipitation due to the interplay of partially saturated flow and gas diffusive transport in the fracture network. The normal non-dimensional parameters like the grid Peclet number and the grid Damköhler numbers are complicated by the fact that we are considering a multicomponent geochemical system here. For example, carbonate is transported both by advection in the aqueous phase, but also by gas diffusion in the gas phase. For carbonate, therefore, it is appropriate to consider a grid Peclet number that compares advective transport in the aqueous phase with diffusive transport in the gas phase. In contrast, magnesium is only present
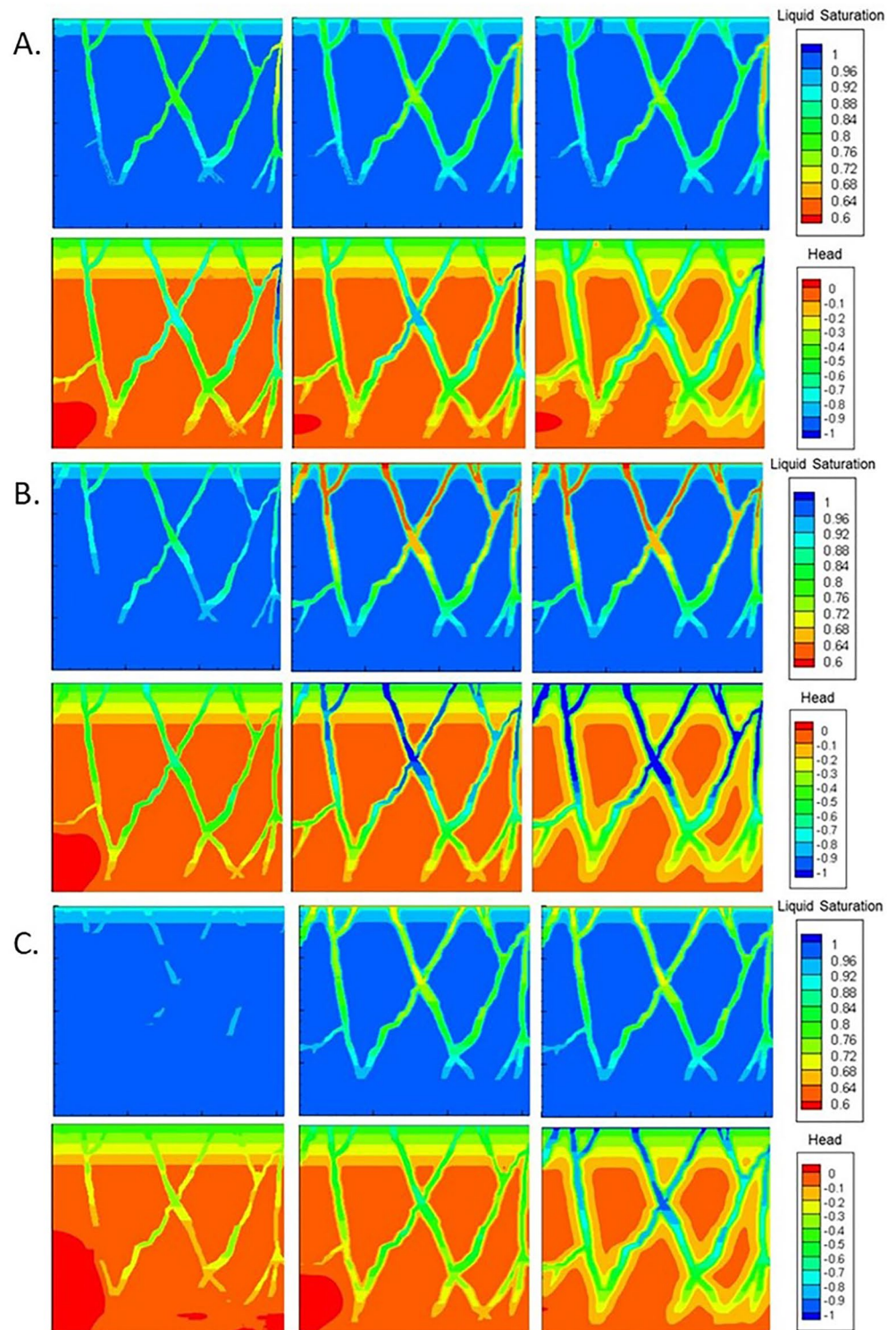
Table 5
Rate Constants and Reactive Surface Areas for the Earth's Critical Zone Simulations

	Rate constant (k_m) mol m^{-2} s^{-1}	Reactive surface area (A_m) m^2 m^{-3}	Initial mineral volume fractions m^3 m^{-3}
Forsterite	10^{-8}	1,000	0.02
Magnesite	10^{-8}	1.00	0.00

Figure 11. Panels showing contour plots of liquid saturation and hydraulic head (m) for the three permeability cases from left to right at 0.0365, 0.365, and 3.65 days. (a) High permeability case ($\phi_F = 10^{-2}$). (b) Medium permeability case ($\phi_F = 10^{-3}$). (c) Low permeability case ($\phi_F = 10^{-4}$).
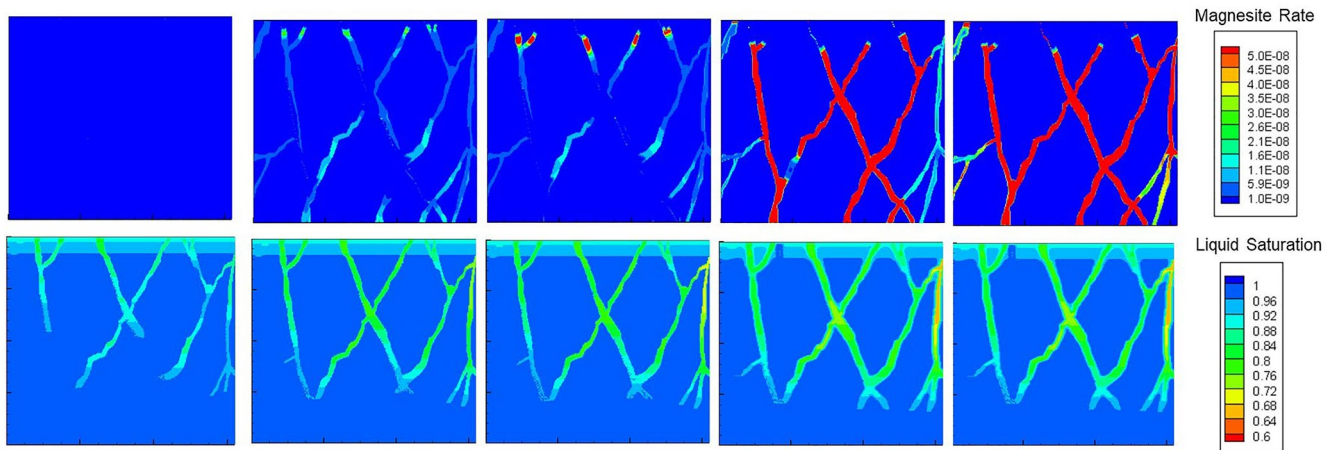
Figure 12. Contour plots at 0.00365, 0.01825, 0.0365, 0.365, and 3.65 days (left to right) of the magnesite precipitation rate (mol m^{-3} s^{-1}) and liquid saturation for the high permeability case ($\phi_F = 10^{-2}$). The simulation assumes a van Genuchten parameter $\alpha = 1.50$.

in the aqueous phase, thus the conventional Peclet number (characteristic time for advective and diffusive transport in the same phase) is relevant.

The total amount of carbon fixed as carbonate for the three different permeability and VG parameter α cases are given in Table 6. A simple relationship based on all of the conditions in the simulations is difficult to develop because of the different stages of approach to steady state. However, the complexity here is also at least partly due to the multicomponent character of the system, with Mg^{2+}present only in the aqueous phase, while CO$_2$ is present in both the gas and aqueous phase. The highest amount of carbon trapping occurs in the high permeability as compared to the medium and low permeability cases, suggesting an important control by advective transport. However, a greater extent of carbon trapping also occurs for the case of VG $\alpha = 1.50$ where the partially saturated zone shows its greatest development (see Table 7 and Figure 11). A possible explanation for this complex behavior is provided in the Discussion section.

4. Discussion

In this study we have considered only a small number of the possible scenarios and environments associated with reactive flow in intersecting fracture networks. Nonetheless, several important generalizations emerge
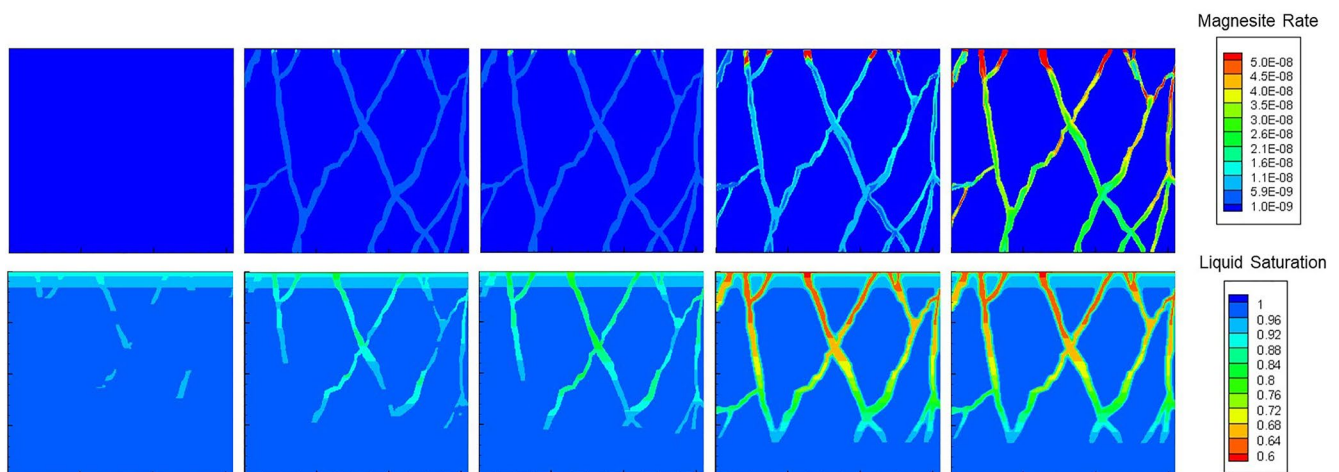

Figure 13. Contour plots at 0.00365, 0.01825, 0.0365, 0.365, and 3.65 days (left to right) of the magnesite precipitation rate (mol m^{-3} s^{-1}) and liquid saturation for the medium permeability case ($\phi_F = 10^{-3}$). The simulation assumes a van Genuchten parameter $\alpha = 1.50$.
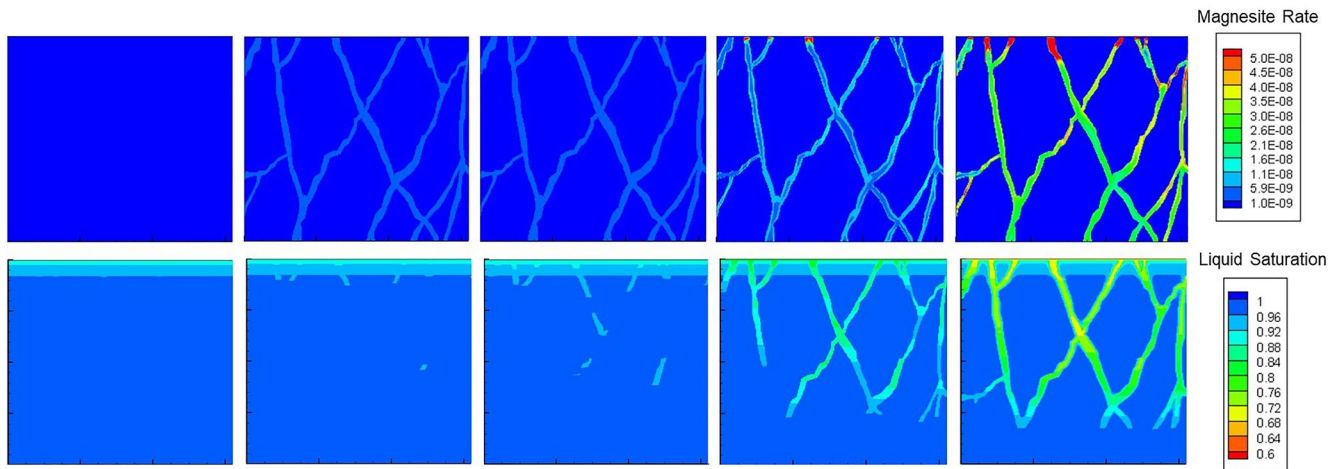
Figure 14. Contour plots at 0.00365, 0.01825, 0.0365, 0.365, and 3.65 days (left to right) of the magnesite precipitation rate (mol m^{-3} s^{-1}) and liquid saturation for the low permeability case ($\phi_F = 10^{-4}$). The simulation assumes a van Genuchten parameter $\alpha = 1.50$.

from the simulations presented here. The most important of these is that the time evolution of physical and chemical properties in the case of an intersecting fracture network is likely very different than what is realized in a more conventional porous medium. This is chiefly because the reaction processes in intersecting fractures can dramatically impact the connectivity of the flow system. This may be particularly the case where mixing, considered in the first set of simulations above, leads to mineral precipitation and/or dissolution in specific fracture segments, while leaving other segments nearly unaffected. This kind of behavior is evident in Figures 7 and 8, where it is clear that the porosity and permeability change will ultimately close down the entire portion of the fracture flow system above and to the right of the intersection point 50 cm above the lower flow boundary.

The time scales for this to occur depend on the geochemical system considered, the flow rates, and the porosity and permeability of the fracture zones themselves. In the case of a fracture network with numerous intersections, there is the possibility of wholesale reorganization of the flow system because the reaction processes can affect very specific segments and relatively small volumes that are critical to the connectivity of the flow system. In this regard, the behavior is akin to what one might find at the pore scale, with local flow and geochemical gradients generating different geochemical conditions in individual pore bodies and pore throats. However, the effect is expected to be more dramatic in fracture networks, since there is very limited diffusive (as opposed to flow) mixing between fractures, in contrast to what is normally expected at the pore scale (Li et al., 2008; Molins et al., 2012, 2014). Thus, the local heterogeneous conditions in the fracture network, often separated by discrete intersections, may be effectively preserved compared to the pore scale where length scales are sufficiently small that diffusive mixing can occur. In fracture networks, the simulations presented here suggest that the time and space evolution of the flow connectivity due to local reactive flow and transport processes may be more important than the effects of the bulk or volume-averaged changes in physical and chemical properties.

In the second set of simulations, we considered the problem of natural weathering of fractured mafic and ultramafic rocks and how this might contribute to mitigation of atmospheric CO$_2$. The case of naturally fractured rock could be taken as a possible end-member against which to compare and evaluate various engineered strategies, as in negative emission technologies (NET). In other words, if one is to quantify an engineered solution in which various reactive phases or rocks (forsterite, basalt, ultramafics) are evaluated, it would be useful and even arguably essential to quantify the "base case" of naturally fractured ultramafic and mafic rocks first.

Table 6
Total Rate in mol/yr for the Simulations Involving Various Permeabilities (Left Column) and Van Genuchten Parameter α (Top Row)

	Lower alpha	Mid alpha	Upper alpha
Lower perm	0.176	0.199	0.201
Medium perm	0.177	0.248	0.269
Higher perm	0.385		0.884

Note. The simulation for high permeability and $\alpha = 1.00$ was not available due to a power shutdown of the workstation. All values (where given) are based on results at 3.65 days.

Table 7

Average Liquid Saturation for the Simulations Involving Various Permeabilities (Left Column) and Van Genuchten Parameter α (Top Row) After 3.65 Days

	Lower alpha	Mid alpha	Upper alpha
Lower perm	0.939	0.860	0.821
Medium perm	0.935	0.824	0.762
Higher perm	0.951		0.862

Note. The simulation for high permeability and $\alpha = 1.00$ was not available due to a power shutdown of the workstation.

The behavior of the partially saturated critical zone is quite complex, as shown in Figures 12–14. Carbon trapping increases with increasing permeability, except for the case of VG $\alpha = 0.50$ for the low and medium permeability cases. This is likely due to the incomplete approach to hydrological steady state at 3.65 days for these two cases. The increase in carbon trapping with higher permeability is due to the higher rate of influx of reactive water into the fracture system. Carbon trapping also increases with increasing values of the VG α parameters. Higher VG α values result in a spatially more extensive partially saturated zone (see Figure 11), which has the effect of expanding the portion of the domain within which CO_2 gas diffusion is important. The correlation with average liquid saturation is less obvious, although this parameter is weighted by the large volume of fully saturated rock matrix. This is shown most clearly by plotting the local grid Peclet number (Figure 15), but using the characteristic time for advective transport of CO_2 in the aqueous phase divided by the characteristic time for CO_2 diffusive gas transport in the gas phase (rather than the CO_2 diffusivity in the aqueous phase, which is 3–4 orders of magnitude slower).

$$\text{Pe}_{\text{grid}} = \frac{\phi v \Delta Z}{S_G^{7/3} \phi^{1/3} D^{g,\text{intrinsic}}} \tag{16}$$

where ΔZ is the grid spacing in the Z direction (1 cm).

As is apparent from Figure 15, for the species CO_2 at least, the system is diffusion controlled— grid Peclet numbers average about 0.01 except at the bottom of the system where it becomes fully saturated. There is of course an exchange between the gas and aqueous phase that follows the Henry's Law constant, but nonetheless, CO_2 transport is clearly more rapid in the gas phase. Thus, a system with higher average gas saturation is expected to show more carbon fixation as carbonate because of the higher CO_2 transport rates in the gas phase. However, it must be recalled that carbonate precipitation requires CO_2 in the aqueous phase (in the form of carbonate ion), but also a metal cation, in this case Mg^{2+}. Mg^{2+}, in contrast to CO_2, is present only in the aqueous phase, so the relevant non-dimensional parameter is the more conventional grid Peclet number that compares advective and diffusive transport in the same (aqueous) phase, or the grid Damköhler number that compares the rate of advective transport to the rate of dissolution or precipitation.

In Figure 16, we see that the forsterite dissolution rate increases with increasing permeability, indicating a partial transport control on the rates of dissolution. Thus, we argue that part of the complexity of the system, which may become even more evident if a broader range of parameter values are considered, is due to the multicomponent nature of the system, with different chemical species (CO_2 and Mg^{2+}) governed by transport rates in different phases.

5. Conclusions

In order to answer a broad scientific question: "*How does mineral precipitation driven by chemical reaction, advection, and gas diffusion interplay with the geometry of natural discrete fracture networks, particularly at*
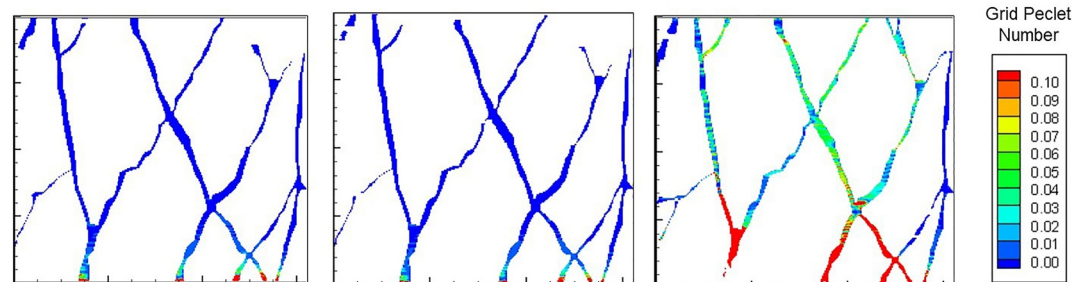

Figure 15. Grid Peclet number defined by Equation 16. Simulations are based on a uniform spacing of 1 cm in the Z direction.
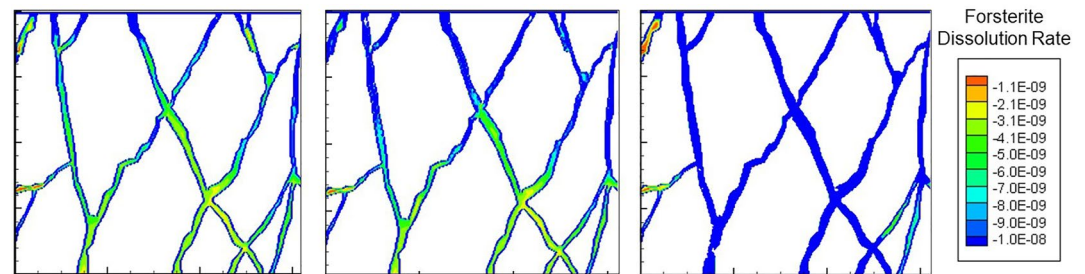
Figure 16. Rate of forsterite dissolution in mol m^{-3} s^{-1} for three different permeability values in the partially saturated critical zone simulations. The most negative numbers represent the highest forsterite dissolution rates.

intersections where coupling of chemical and physical processes is most important?," we have conducted two sets of simulations of a natural intersecting fracture network taken from outcrop photographs. Our modeling considers realistic geometry of intersecting rough fractures and its interplay with advection, gas diffusion, and mineral dissolution and precipitation. Based on the first set of simulations on mixing, we have reached the following important conclusion:

- Reaction-induced changes in fracture segment properties that are primarily affected by the fracture intersections can substantially alter the connectivity of the system, an impact that likely exceeds the effect(s) of changes in the geometry, and bulk physical, and chemical properties.

A good example is provided by the case where fluid mixing at a fracture intersection results in mineral precipitation (magnesite in this example) in one fracture segment, while leaving other segments nearly unaffected. The time scales in an intersecting fracture network, however, are likely to be shorter than would be the case for nearly homogeneous porous media, since local reaction-induced changes in the fracture can have an outsized impact on the flow and transport regime through modifications of the connectivity associated with mineral precipitation and dissolution at or close to fracture intersections. The reactive transport processes taking place in the fracture network present the possibility of wholesale reorganization of the flow system due to changes in connectivity.

In the second set of simulations, we considered the problem of natural weathering of fractured mafic and ultramafic rocks and how this could contribute to mitigation of atmospheric CO_2. The system shows complex behavior that is due in part to the multicomponent nature of the overall incongruent reaction, with forsterite dissolving to release Mg^{2+} into solution while CO_2 is transported in both the gas and aqueous phase in the partially saturated portion of the critical zone. The major research finding based on these simulations is that:

- Under various flow conditions, decreasing water content (or increasing gas saturation) can result in increased fixation of carbon in carbonate form. At higher flow rates, the rate of dissolution of the primary mineral(s) can increase the rate at which the cation Mg^{2+} is made available for precipitation in the form of magnesite.

Thus, the disparate behavior of CO_2 and Mg^{2+} can result in complex behavior that may make it difficult to correlate carbon fixation potential with a single parameter. Further, we conclude that:

- The amounts of carbon that can be sequestered are modest, but the naturally fractured domain, even if considered only with a computational approach, provides a useful "base case" for the future design of efficient strategies for carbon trapping and mitigation.

The numerical experiments presented here have not yet been calibrated or validated against a natural field system, although this should be a prime objective of future research to the extent that the funding agencies can be talked into investing in detailed field studies of carbon trapping in the critical zone. But reactive transport modeling has now come far enough that it represents at least a useful first step in designing CO_2 mitigation strategies.

Data Availability Statement

The research data for this study are available from a DRYAD data repository, Steefel and Hu (2022, https://doi.org/10.7941/D1VK7X). The source code for CrunchTope used to run the simulations can be accessed from Steefel et al. (2022) https://doi.org/10.5281/zenodo.6459627.

References

Ameli, P., Elkhoury, J. E., Morris, J. P., & Detwiler, R. L. (2014). Fracture permeability alteration due to chemical and mechanical processes: A coupled high-resolution model. *Rock Mechanics and Rock Engineering*, *47*(5), 1563–1573. https://doi.org/10.1007/s00603-014-0575-z

Aradóttir, E. S. P., Sonnenthal, E. L., Björnsson, G., & Jónsson, H. (2012). Multidimensional reactive transport modeling of CO_2 mineral sequestration in basalts at the Hellisheidi geothermal field, Iceland. *International Journal of Greenhouse Gas Control*, *9*, 24–40. https://doi.org/10.1016/j.ijggc.2012.02.006

Beckingham, L. E., Mitnick, E. H., Steefel, C. I., Zhang, S., Voltolini, M., Swift, A. M., et al. (2016). Evaluation of mineral reactive surface area estimates for prediction of reactivity of a multi-mineral sediment. *Geochimica et Cosmochimica Acta*, *188*, 310–329. https://doi.org/10.1016/j.gca.2016.05.040

Beckingham, L. E., Steefel, C. I., Swift, A. M., Voltolini, M., Yang, L., Anovitz, L. M., et al. (2017). Evaluation of accessible mineral surface areas for improved prediction of mineral reaction rates in porous media. *Geochimica et Cosmochimica Acta*, *205*, 31–49. https://doi.org/10.1016/j.gca.2017.02.006

Berkowitz, B. (2002). Characterizing flow and transport in fractured geological media: A review. *Advances in Water Resources*, *25*(8–12), 861–884. https://doi.org/10.1016/s0309-1708(02)00042-8

Blessent, D., Jørgensen, P. R., & Therrien, R. (2014). Comparing discrete fracture and continuum models to predict contaminant transport in fractured porous media. *Groundwater*, *52*(1), 84–95. https://doi.org/10.1111/gwat.12032

Boisson, A., Guihéneuf, N., Perrin, J., Bour, O., Dewandel, B., Dausse, A., et al. (2015). Determining the vertical evolution of hydrodynamic parameters in weathered and fractured south Indian crystalline-rock aquifers: Insights from a study on an instrumented site. *Hydrogeology Journal*, *23*(4), 757–773. https://doi.org/10.1007/s10040-014-1226-x

Brantley, S. L., Goldhaber, M. B., & Vala Ragnarsdottir, K. (2007). Crossing disciplines and scales to understand the critical zone. *Elements*, *3*(5), 307–314. https://doi.org/10.2113/gselements.3.5.307

Campbell, J. S., Foteinis, S., Furey, V., Hawrot, O., Pike, D., Aeschlimann, S., et al. (2022). Geochemical negative emissions technologies: Part I. Review. *Frontiers in Climate*, *4*, 879133. https://doi.org/10.3389/fclim.2022.879133

Celia, M. A., Bouloutas, E. T., & Zarba, R. L. (1990). A general mass-conservative numerical solution for the unsaturated flow equation. *Water Resources Research*, *26*(7), 1483–1496. https://doi.org/10.1029/wr026i007p01483

Chambon, J. C., Broholm, M. M., Binning, P. J., & Bjerg, P. L. (2010). Modeling multi-component transport and enhanced anaerobic dechlorination processes in a single fracture–clay matrix system. *Journal of Contaminant Hydrology*, *112*(1–4), 77–90. https://doi.org/10.1016/j.jconhyd.2009.10.008

Chen, F., Falta, R. W., & Murdoch, L. C. (2012). Numerical analysis of contaminant removal from fractured rock during boiling. *Journal of Contaminant Hydrology*, *134*, 12–21. https://doi.org/10.1016/j.jconhyd.2012.04.004

Chen, Y. F., Ye, Y., Hu, R., Yang, Z., & Zhou, C. B. (2022). Modeling unsaturated flow in fractured rocks with scaling relationships between hydraulic parameters. *Journal of Rock Mechanics and Geotechnical Engineering*. https://doi.org/10.1016/j.jrmge.2022.02.008

Crandall, D., Hajirezaie, S., Peters, C., Swift, A., Sheets, J., Stack, A., et al. (2017). *Mineral precipitation in fractures: Multiscale imaging and geochemical modeling (No. NETL-PUB-21613)*. National Energy Technology Laboratory (NETL).

Detwiler, R. L. (2008). Experimental observations of deformation caused by mineral dissolution in variable-aperture fractures. *Journal of Geophysical Research*, *113*(B8), B08202. https://doi.org/10.1029/2008JB005697

Dixon, J. L., Heimsath, A. M., & Amundson, R. (2009). The critical role of climate and saprolite weathering in landscape evolution. *Earth Surface Processes and Landforms*, *34*(11), 1507–1521. https://doi.org/10.1002/esp.1836

Feng, J., Zhang, X., Luo, P., Li, X., & Du, H. (2019). Mineral filling pattern in complex fracture system of carbonate reservoirs: Implications from geochemical modeling of water-rock interaction. *Geofluids*, *2019*, 1–19. https://doi.org/10.1155/2019/3420142

Figueiredo, B., Tsang, C. F., Rutqvist, J., & Niemi, A. (2017). Study of hydraulic fracturing processes in shale formations with complex geological settings. *Journal of Petroleum Science and Engineering*, *152*, 361–374. https://doi.org/10.1016/j.petrol.2017.03.011

Giammar, D. E., Bruant, R. G., Jr., & Peters, C. A. (2005). Forsterite dissolution and magnesite precipitation at conditions relevant for deep saline aquifer storage and sequestration of carbon dioxide. *Chemical Geology*, *217*(3–4), 257–276. https://doi.org/10.1016/j.chemgeo.2004.12.013

Hänchen, M., Prigiobbe, V., Storti, G., Seward, T. M., & Mazzotti, M. (2006). Dissolution kinetics of fosteritic olivine at 90–150°C including effects of the presence of CO_2. *Geochimica et Cosmochimica Acta*, *70*(17), 4403–4416. https://doi.org/10.1016/j.gca.2006.06.1560

Hu, M., & Rutqvist, J. (2020). Numerical manifold method modeling of coupled processes in fractured geological media at multiple scales. *Journal of Rock Mechanics and Geotechnical Engineering*, *12*(4), 667–681. https://doi.org/10.1016/j.jrmge.2020.03.002

Hu, M., & Rutqvist, J. (2022). Multi-scale coupled processes modeling of fractures as porous, interfacial and granular systems from rock images with the numerical manifold method. *Rock Mechanics and Rock Engineering*, *55*(5), 3041–3059. https://doi.org/10.1007/s00603-021-02455-6

Hu, M., Rutqvist, J., & Steefel, C. I. (2021). Mesh generation and optimization from digital rock fractures based on neural style transfer. *Journal of Rock Mechanics and Geotechnical Engineering*, *13*(4), 912–919.

Hu, M., Rutqvist, J., & Wang, Y. (2016). A practical model for flow in discrete-fracture porous media by using the numerical manifold method. *Advances in Water Resources*, *97*, 38–51. https://doi.org/10.1016/j.advwatres.2016.09.001

Hu, M., Rutqvist, J., & Wang, Y. (2017). A numerical manifold method model for analyzing fully coupled hydro-mechanical processes in porous rock masses with discrete fractures. *Advances in Water Resources*, *102*, 111–126. https://doi.org/10.1016/j.advwatres.2017.02.007

Hu, M., Steefel, C. I., & Rutqvist, J. (2021). Microscale mechanical-chemical modeling of granular salt: Insights for creep. *Journal of Geophysical Research: Solid Earth*, *126*(12), e2021JB023112. https://doi.org/10.1029/2021jb023112

Hu, Q., Kneafsey, T. J., Trautz, R. C., & Wang, J. S. (2002). Tracer penetration into welded tuff matrix from flowing fractures. *Vadose Zone Journal*, *1*(1), 102–112. https://doi.org/10.2136/vzj2002.0102

Hyman, J. D., & Jiménez-Martínez, J. (2018). Dispersion and mixing in three-dimensional discrete fracture networks: Nonlinear interplay between structural and hydraulic heterogeneity. *Water Resources Research*, *54*(5), 3243–3258. https://doi.org/10.1029/2018wr022585

Jones, T. A., & Detwiler, R. L. (2019). Mineral precipitation in fractures: Using the level-set method to quantify the role of mineral heterogeneity on transport properties. *Water Resources Research*, *55*(5), 4186–4206. https://doi.org/10.1029/2018wr024287

Laubach, S. E., Lander, R. H., Criscenti, L. J., Anovitz, L. M., Urai, J. L., Pollyea, R. M., et al. (2019). The role of chemistry in fracture pattern development and opportunities to advance interpretations of geological materials. *Reviews of Geophysics*, *57*(3), 1065–1111. https://doi.org/10.1029/2019rg000671

Li, L., Steefel, C. I., & Yang, L. (2008). Scale dependence of mineral dissolution rates within single pores and fractures. *Geochimica et Cosmochimica Acta*, *72*(2), 360–377. https://doi.org/10.1016/j.gca.2007.10.027

Li, Z., Özgen-Xian, I., & Maina, F. Z. (2021). A mass-conservative predictor-corrector solution to the 1D Richards equation with adaptive time control. *Journal of Hydrology*, *592*, 125809. https://doi.org/10.1016/j.jhydrol.2020.125809

Millington, R. J., & Quirk, J. P. (1961). Permeability of porous solids. *Transactions of the Faraday Society*, *57*, 1200–1207. https://doi.org/10.1039/tf9615701200

Molins, S., Trebotich, D., Steefel, C. I., & Shen, C. (2012). An investigation of the effect of pore scale flow on average geochemical reaction rates using direct numerical simulation. *Water Resources Research*, *48*(3), W03527. https://doi.org/10.1029/2011wr011404

Molins, S., Trebotich, D., Yang, L., Ajo-Franklin, J. B., Ligocki, T. J., Shen, C., & Steefel, C. I. (2014). Pore-scale controls on calcite dissolution rates from flow-through laboratory and numerical experiments. *Environmental Science & Technology*, *48*(13), 7453–7460. https://doi.org/10.1021/es5013438

Mualem, Y. (1976). A new model for predicting the hydraulic conductivity of unsaturated porous media. *Water Resources Research*, *12*(3), 513–522. https://doi.org/10.1029/wr012i003p00513

Noiriel, C., Seigneur, N., Le Guern, P., & Lagneau, V. (2021). Geometry and mineral heterogeneity controls on precipitation in fractures: An X-ray micro-tomography and reactive transport modeling study. *Advances in Water Resources*, *152*, 103916. https://doi.org/10.1016/j.advwatres.2021.103916

Novitsky, C. G., Steven Holbrook, W., Carr, B. J., Pasquet, S., Okaya, D., & Flinchum, B. A. (2018). Mapping inherited fractures in the critical zone using seismic anisotropy from circular surveys. *Geophysical Research Letters*, *45*(7), 3126–3135. https://doi.org/10.1002/2017GL075976

Owen, R., Maziti, A., & Dahlin, T. (2007). The relationship between regional stress field, fracture orientation and depth of weathering and implications for groundwater prospecting in crystalline rocks. *Hydrogeology Journal*, *15*(7), 1231–1238. https://doi.org/10.1007/s10040-007-0224-7

Rempe, D. M., & Dietrich, W. E. (2014). A bottom-up control on fresh-bedrock topography under landscapes. *Proceedings of the National Academy of Sciences of the United States of America*, *111*(18), 6576–6581. https://doi.org/10.1073/pnas.1404763111

Shapiro, A. M., Hsieh, P. A., Burton, W. D., & Walsh, G. J. (2007). Integrated multi-scale characterization of ground-water flow and chemical transport in fractured crystalline rock at the Mirror Lake site, New Hampshire. In D. W. Hyndman, F. D. Day-Lewis, & K. Singha (Eds.), *Subsurface hydrology: Data integration for properties and processes, geophysical monograph series* (Vol. 171, pp. 201–225). American Geophysical Union. https://doi.org/10.1029/171GM15

Singurindy, O., & Berkowitz, B. (2005). The role of fractures on coupled dissolution and precipitation patterns in carbonate rocks. *Advances in Water Resources*, *28*(5), 507–521. https://doi.org/10.1016/j.advwatres.2005.01.002

Steefel, C., & Hu, M. (2022). Reactive transport modeling of mineral precipitation and carbon trapping in discrete fracture networks [Dataset]. Dryad. https://doi.org/10.7941/D1VK7X

Steefel, C. I., Appelo, C. A. J., Arora, B., Jacques, D., Kalbacher, T., Kolditz, O., et al. (2015). Reactive transport codes for subsurface environmental simulation. *Computational Geosciences*, *19*(3), 445–478. https://doi.org/10.1007/s10596-014-9443-x

Steefel, C. I., & Lasaga, A. C. (1994). A coupled model for transport of multiple chemical species and kinetic precipitation/dissolution reactions with application to reactive flow in single phase hydrothermal systems. *American Journal of Science*, *294*(5), 529–592. https://doi.org/10.2475/ajs.294.5.529

Steefel, C. I., Li, Z., & Stolze, L. (2022). *CISteefel/CrunchTope: CrunchTope-v2.0.1 (v2.0.1)*. Zenodo. https://doi.org/10.5281/zenodo.6459627

Steefel, C. I., & Lichtner, P. C. (1994). Diffusion and reaction in rock matrix bordering a hyperalkaline fluid-filled fracture. *Geochimica et Cosmochimica Acta*, *58*(17), 3595–3612. https://doi.org/10.1016/0016-7037(94)90152-x

Steefel, C. I., & Lichtner, P. C. (1998). Multicomponent reactive transport in discrete fractures: II: Infiltration of hyperalkaline groundwater at Maqarin, Jordan, a natural analogue site. *Journal of Hydrology*, *209*(1–4), 200–224. https://doi.org/10.1016/s0022-1694(98)00173-5

Steefel, C. I., & Yang, L. (2021). Secondary magnesite formation from forsterite under CO_2 sequestration conditions via coupled heterogeneous nucleation and crystal growth. *Geochimica et Cosmochimica Acta*, *311*, 29–42. https://doi.org/10.1016/j.gca.2021.07.030

Van Genuchten, M. T. (1980). A closed-form equation for predicting the hydraulic conductivity of unsaturated soils. *Soil Science Society of America Journal*, *44*(5), 892–898. https://doi.org/10.2136/sssaj1980.03615995004400050002x

Wang, F., & Giammar, D. E. (2013). Forsterite dissolution in saline water at elevated temperature and high CO_2 pressure. *Environmental Science & Technology*, *47*(1), 168–173. https://doi.org/10.1021/es301231n

Witherspoon, P. A., Wang, J. S., Iwai, K., & Gale, J. E. (1980). Validity of cubic law for fluid flow in a deformable rock fracture. *Water Resources Research*, *16*(6), 1016–1024. https://doi.org/10.1029/wr016i006p01016

Xiong, W., & Giammar, D. (2014). Forsterite carbonation in zones with transport limited by diffusion. *Environmental Science and Technology Letters*, *1*(8), 333–338. https://doi.org/10.1021/ez500182s

Xiong, W., Wells, R. K., Horner, J. A., Schaef, H. T., Skemer, P. A., & Giammar, D. E. (2018). CO_2 mineral sequestration in naturally porous basalt. *Environmental Science and Technology Letters*, *5*(3), 142–147. https://doi.org/10.1021/acs.estlett.8b00047

Zimmerman, R. W., & Bodvarsson, G. S. (1996). Hydraulic conductivity of rock fractures. *Transport in Porous Media*, *23*(1), 1–30. https://doi.org/10.1007/bf00145263

Zimmerman, R. W., & Yeo, I. W. (2000). Fluid flow in rock fractures: From the Navier-Stokes equations to the cubic law. *Geophysical Monograph-American Geophysical Unio*n, *122*, 213–224.